Title

Simultaneous multiagent hyperpolarized 13C perfusion imaging

Journal

Magnetic Resonance in Medicine, 72(6)

ISSN

0740-3194

Authors

von Morze, Cornelius
Bok, Robert A
Reed, Galen D
et al.

Publication Date

2014-12-01

DOI

10.1002/mrm.25071

Peer reviewed

Published in final edited form as:
Magn Reson Med. 2014 December ; 72(6): 1599–1609. doi:10.1002/mrm.25071.

Simultaneous Multiagent Hyperpolarized ^{13}C Perfusion Imaging

Cornelius von Morze[1,*], **Robert A. Bok**[1], **Galen D. Reed**[1], **Jan Henrik Ardenkjaer-Larsen**[2,3], **John Kurhanewicz**[1], and **Daniel B. Vigneron**[1]

[1]Department of Radiology and Biomedical Imaging, University of California, San Francisco, California, USA.

[2]GE Healthcare, Brøndby, Denmark.

[3]Department of Electrical Engineering, Technical University of Denmark, Lyngby, Denmark.

Abstract

Purpose—To demonstrate simultaneous hyperpolarization and imaging of three ^{13}C-labeled perfusion MRI contrast agents with dissimilar molecular structures ([^{13}C]urea, [^{13}C]hydroxymethyl cyclopropane, and [^{13}C]t-butanol) and correspondingly variable chemical shifts and physiological characteristics, and to exploit their varying diffusibility for simultaneous measurement of vascular permeability and perfusion in initial preclinical studies.

Methods—Rapid and efficient dynamic multislice imaging was enabled by a novel pulse sequence incorporating balanced steady state free precession excitation and spectral-spatial readout by multiband frequency encoding, designed for the wide, regular spectral separation of these compounds. We exploited the varying bilayer permeability of these tracers to quantify vascular permeability and perfusion parameters simultaneously, using perfusion modeling methods that were investigated in simulations. “Tripolarized” perfusion MRI methods were applied to initial preclinical studies with differential conditions of vascular permeability, in normal mouse tissues and advanced transgenic mouse prostate tumors.

Results—Dynamic imaging revealed clear differences among the individual tracer distributions. Computed permeability maps demonstrated differential permeability of brain tissue among the tracers, and tumor perfusion and permeability were both elevated over values expected for normal tissues.

Conclusion—Tripolarized perfusion MRI provides new molecular imaging measures for specifically monitoring permeability, perfusion, and transport simultaneously in vivo.

Keywords

perfusion imaging; permeability; hyperpolarized; ^{13}C; DNP; prostate cancer

[*]Correspondence to: Cornelius von Morze, Ph.D., Department of Radiology and Biomedical Imaging, University of California, San Francisco, 1700 Fourth Street, Byers Hall Suite 102 San Francisco, CA 94158. cornelius.vonmorze@ucsf.edu.

INTRODUCTION

Perfusion images reflect both modality-dependent physical contrast mechanisms and tracer physiology, because molecular structure dictates the biodistribution of the contrast agent. Dissolution dynamic nuclear polarization (DNP) technology (1) has enabled development of three ^{13}C-labeled tracers that are suitable for hyperpolarized (HP) perfusion MRI, based on the key criteria of large DNP enhancements (>10,000 fold), long T_1 relaxation time, negligible metabolism, and low toxicity: [^{13}C]urea (T_1 = 47 s in solution at 3T, δ = 163 ppm) (2, 3); [^{13}C]HMCP (hydroxymethyl cyclopropane [also known as HP001] or bis-1,1-(hydroxymethyl)-[1-^{13}C]cyclopropaned_8, T_1 = 95 s, δ = 23 ppm) (4–6); and [^{13}C]t-butanol (i.e., [2-^{13}C]2-methyl-2-propanol-d_9, T_1 = 46 s, δ = 70 ppm) (7). As a result of their dissimilar molecular structures (Fig. 1), these molecules exhibit broad chemical shift dispersion and have widely different distribution in vivo due to varying lipid bilayer permeability and transport. For example, urea (octanol-water coefficient log K_{OW} = −2.80) is highly polar and has correspondingly low bilayer permeability, whereas t-butanol (log K_{OW} = 0.35) is considered freely diffusible (7, 8). As a biologically significant endogenous molecule, however, urea is rapidly transported across cell membranes in red blood cells and in the inner medullary collecting ducts of the kidneys via specific facilitated transport proteins that are vital for the production of concentrated urine (9, 10).

HP perfusion MRI has the desirable features of direct proportionality of signal to tracer concentration (times polarization) and higher diffusibility than many other common perfusion imaging contrast agents, as well as potentially reduced nephrotoxicity (11). This proportionality could allow improved input function estimation, potentially leading to improved quantification of blood flow and other hemodynamic parameters using MRI (12). Rapid high dose infusions of urea are historically known to be safe in humans, exemplified by the “urea washout pyelogram” diagnostic imaging test (13), and ultrahigh doses (e.g., 1 g/kg) are sometimes used clinically for therapeutic osmotic effects (14). The toxicity of t-butanol, which is minimal and comparable to ethanol in the acute setting, has been studied extensively due to its role as an important intermediate in industrial syntheses (15). The safety profile of HMCP requires further study, but no acute toxicities have been reported in preclinical HP studies to date at doses up to −220 mg/kg (4, 5).

The potential value of these three HP perfusion tracers has been investigated individually through initial preclinical application studies focused on neuroimaging (4, 7), cancer imaging (3, 6), and renal functional imaging (16). To obtain an unprecedented level of physiologic detail, in this study we investigated co-hyperpolarization (17) and simultaneous imaging of these three distinct “tripolarized” perfusion tracers in a single study. Although quantification of perfusion using HP ^{13}C MRI has been demonstrated previously (3), we exploited the varying lipophilicity of these tracers to quantify both vascular permeability and perfusion parameters simultaneously, a major outstanding goal of perfusion imaging research (18). We also investigated initial applications of these methods in two initial preclinical studies with differential conditions of vascular permeability, in normal mouse tissues, and in advanced transgenic mouse prostate tumors. The overall scope of this work thus encompasses both a technical description of the new methods for copolarization and simultaneous imaging of these three HP tracers, and their initial application to preclinical

murine studies that exploit their varying diffusibility for simultaneous estimation of permeability and perfusion.

This tandem multiagent approach capitalizes on a singular advantage of MRI over other medical imaging modalities to resolve multiple tracers based on frequency differences. However, simultaneous MRI of multiple tracers is traditionally very slow, because it relies on spectroscopic imaging methods such as chemical shift imaging; therefore, reasonable spatiotemporal resolution and coverage cannot be achieved within the limited temporal window dictated by the rapid T_1 decay of HP magnetization. The performance of imaging of multiple HP compounds can be greatly enhanced with customized pulse sequence approaches (19–23). In particular, we employed the method of multiband frequency encoding (24), which realizes large advantages with wide spectral separation, as for these ^{13}C tracers. Given the long T_2 relaxation times of these agents (25), an efficient use of the initial magnetization is also desirable. Balanced steady state free precession (SSFP) enables both rapid and efficient imaging for HP perfusion applications (2–6), but its spectral response must be considered (26–28). In this study, we capitalized on the wide, regular spectral separation of the three aforementioned tracers to achieve rapid dynamic imaging of all these contrast agents simultaneously with full body coverage in preclinical murine imaging studies using balanced SSFP and multiband frequency encoding.

METHODS

Pulse Sequence Design

The periodic SSFP response of HP magnetization was modeled in Bloch simulations as a function of Larmor frequency offset. The magnetization was evolved over 20 pulses with flip angle $\alpha = 20°$. An initial $\alpha/2$ pulse was applied to catalyze a “pseudo steady state”, and successive pulses were phase modulated by 180°(i.e., $\pm\alpha$) (2–5). A TR was selected so that the on-resonance spectral response would be almost exactly replicated for each of the three compounds. This was determined from chemical shift differences among the agents, which were calculated from a HP trial run with non-localized spectroscopy. Since the spectral separation between HMCP and urea (4495 Hz) is nearly an exact integer multiple of the separation between HMCP and t-butanol (1497 Hz), an appropriate center frequency near HMCP and a TR of a multiple of 1/1498 Hz (specifically 18.0 ms) results in replication of the spectral response for all three compounds to within ±1 Hz. A minimum usable bandwidth of 16 Hz (0.5 ppm) was obtained for each compound, where signal variation as a function of frequency and oscillation of signal magnitude over the phase encoding steps was <10% (Fig. 2). While this TR is prohibitively long for ^1H SSFP at 3T due to banding, because of the 4× lower gyromagnetic ratio of carbon, it is actually equivalent in terms of artifact level to 4.5 ms for protons, a reasonable value (29). The measured spectral shifts were also used to set up the modified readout filter (6.0 kHz) and reconstruction pixel shifts for multiband frequency encoding and to compensate for tilted excitation profiles for the individual compounds along the slice direction due to chemical shift misregistration. Flip angles were ramped over the dynamic acquisitions to maximize the imaging window. The flip angles were as follows: $\alpha = 0.5°$, 1°, 2°, 4°, 6°, 9°, 12°, 16°, 20°, 25°, 32°, 41°, 55°, 70°, 100°, 130°.

Hyperpolarization

Methods of dissolution DNP and co-hyperpolarization of multiple agents were similar to those described previously (1, 6, 17). [^{13}C]urea (Sigma, St. Louis, Missouri, USA) was dissolved in glycerol (6.4 M), with 18 mM trityl radical OX063 and 1.0 mM Dotarem (Guerbet, Roissy, France). HMCP was mixed with water in a ratio of 2.78:1 by weight, with 19 mM OX063 (Oxford Instruments, Tubney Woods, UK) and 1.2 mM Dotarem. [^{13}C]t-butanol (Sigma) was mixed with glycerol (50:50 by weight), with 15 mM “FINLAND” trityl radical (Oxford Instruments) and 1.0 mM Dotarem. For each study, 0.5 mmol each of [^{13}C]HMCP, [^{13}C]t-butanol, and [^{13}C]urea were loaded in that order into the sample cup of the Hypersense DNP polarizer (Oxford Instruments, Abingdon UK). Each compound was loaded into the sample cup individually, with freezing by immersion in liquid nitrogen at each stage to prevent mixing. Dissolution in 4.5 mL phosphate-buffered saline resulted in a solution isomolar for each compound at 110 mM, close to physiologic pH (~7.3) and slightly hypertonic.

MRI Experiments

MRI hardware consisted of a 3T MRI scanner (GE Healthcare, Waukesha, Wisconsin, USA) equipped with multinuclear capability and a custom dual-tuned volume coil for imaging mice. Feasibility of the pulse sequence methods was first tested by imaging a pair of vial phantoms containing enriched [^{13}C]urea in glycerol (6 M) and HMCP in water (5 M), respectively, both doped with Magnevist (Bayer, Leverkusen, Germany) (1% by volume). Subsequently, four normal mice and four transgenic mice with prostate cancer (transgenic adenocarcinoma of mouse prostate [TRAMP]) were imaged (30). Mice were maintained under isoflurane anesthesia during these experiments and were placed on a heated water pad inside the scanner. For each study, the mouse was injected over 12 s with 350 μL of copolarized material. The ^{13}C pulse sequence parameters were as follows: axial two-dimensional balanced SSFP; matrix = 16 × 16; field of view (FOV) = 4 cm; slice thickness = 10 mm; echo time (TE)/repetition time (TR) = 9.0/18.0 ms. The nominal spatial resolution was 2.5 × 2.5 × 10 mm or 0.0625 cm^3. The minimum filter bandwidth, which for multiband frequency encoding must be set wider than the conventional imaging setting of $\gamma G \cdot FOV$, is $(\delta_{max} - \delta_{min} + \Delta\delta_{min})\gamma B_0$ = 6.0 kHz over 64 total readout points covering all three agents. The transmit gain for all experiments was set using signal from a urea reference vial placed adjacent to the animal. Dynamic multislice imaging commenced at the start of injection and was repeated every 3.8 s over 57 s. Slice selective excitation by a sinc pulse of duration 2.63 ms (bandwidth = 1500 Hz) and centered near HMCP resulted in offsets of approximately one slice for t-butanol and three slices for urea, due to chemical shift misregistration of the transmit profile, which was corrected in reconstruction.

Three extra slices beyond the animal were acquired to correct for this effect. Axial multislice T_2-weighted fast spin echo ^{1}H images were acquired for overlay of the dynamic HP images (matrix = 192 × 192; FOV = 10 cm; slice thickness = 2 mm; TE/TR = 79.7/628 ms; bandwidth = ±83.3 kHz; number of excitations = 6). Axial three-dimensional time-of-flight (TOF) MR angiography (MRA) images were also acquired to better define input vessel size, as required for better quantification of the input function given partial voluming in the ^{13}C

images (matrix = 160 × 128 × 32; FOV = 8 cm; slice thickness = 2 mm; TE/TR = 2.8/20 ms; α = 13°; bandwidth = ±30 kHz).

Perfusion and Permeability Modeling

Tripolarized dynamic perfusion data in normal mouse tissues (brain and liver) and abnormal TRAMP tumor tissues were modeled according to a single-compartment model governed by the differential equation

$$\frac{dC_{tissue}(t)}{dt} = EFC_{plasma}(t) - \frac{EF}{V_T}C_{tissue}(t) \quad [1]$$

where C_{tissue} is the tracer concentration in tissue (MR signal/mL) and C_{plasma} is the arterial input function (MR signal/mL), while F is the tissue perfusion (mL/mL/s), E is the extraction fraction of each agent (unitless), and V_T is the distribution volume of each agent (mL/mL). All tracer dynamic curves were fit by joint nonlinear least squares to its solution,

$$C_{tissue}(t) = (1 - v_b)EF\exp(-EFt/V_T \otimes C_{plasma}(t) + v_b C_{plasma} \quad [2]$$

including a blood volume v_b mL/mL). The extraction fraction E was modeled as a function of vessel permeability surface (PS) product (mL/mL/s), by $E = PS/(PS + F)$. Due to impermeability of red blood cells to HMCP, its arterial input function was corrected by dividing by (*1 - hematocrit, estimated*) or 0.55. These methods are based on a standard single compartment model as commonly applied in other modalities such as dynamic contrast-enhanced MRI and blood flow positron emission tomography (PET) (12). To take maximal advantage of the high diffusibility of t-butanol, its dynamic data were first separately fit (assuming E = 1, as a freely diffusible tracer) to estimate the perfusion F, $V_{T,t\text{-}butanol}$, and v_b. Subsequently, PS products and distribution volumes of the remaining tracers were jointly estimated using all of the data, with F, $V_{T,t\text{-}butanol}$, and v_b established by the initial separate fit (to within bounds of ±10%). Tissues were manually defined on the T_2 images for region of interest analysis, and corresponding dynamic signal curves were generated, as well as image-derived arterial input functions from a segment of the aorta. Due to partial voluming of input vessels in the ^{13}C images, for the purpose of perfusion quantification, input vessel size was estimated using the TOF MRA data. Although the ramped flip angle scheme maintains a relatively consistent proportionality of signal to tracer concentration, dynamic data were first compensated for relaxation effects by filtering the data according to the expected signal level within the ramped flip angle scheme. This was achieved by estimating the signal for each tracer at the center of each k-space frame (M_n) following the preceding n = 8 pulses according to the formula previously given by Svensson et al. (5):

$$M_n = M_{z,0}\sin\frac{\alpha}{2}\left((E1\cos\frac{\alpha}{2})^2 + (E2\cos\frac{\alpha}{2})^2\right)^n \quad [3]$$

where $M_{z,0}$ is the longitudinal magnetization at the start of each train, $E1 = \exp(-TE/T1)$, and $E2 = \exp(-TE/T2)$. The effect of prior pulse trains and relaxation between dynamic repetitions was also included (3). The assumed approximate relaxation times in tissue were:

$T_{1,HMCP} = T_{1,t\text{-butanol}} = 32$s, $T_{1,urea} = 18$ s, $T_{2,HMCP} = T_{2,t\text{-butanol}} = 500$ ms, $T_{2,urea} = 200$ ms. Since deviation from these expected T_1 and/or T_2 relaxation times within tissues could affect the data analysis, potential effects were investigated in the simulations described below. Because blood concentration was sampled close to the tissue of interest and frequently in comparison with expected T_1 relaxation times in blood, differential relaxation between blood and tissues would not be expected to have a significant effect on the results. Assuming short transit from the input blood to tissue, the majority of any effect of differential relaxation in blood is removed in the step of sampling the input function.

Simulations

The above perfusion modeling methods were studied in computer simulations. Virtual tracer concentration time curves were generated by convolving three tracer residue functions, defined as above by $EF\exp(EFt/V_T)$, with a gamma-variate arterial input function known to approximate the arterial concentration curve for the injection procedure as described previously (3), defined by

$$C_{plasma}(t \geq 0) = A_0(t - t_0)^{\alpha}\exp(-(t - t_0)/\beta) \quad [4]$$

where t_0 is the tracer arrival time (with $\alpha = 3.3$, $\beta = 4.0$). While the perfusion, distribution, and blood volumes were held constant ($F = 60$ mL/dL/min, $V_{T,HMCP} = 0.2$, $V_{T,t\text{-butanol}} = 0.45$, $V_{T,urea} = 0.12$, $v_b = 0$), three biological sets of conditions corresponding to low ($F = 5$ $PS_{HMCP} = 25$ PS_{urea}), intermediate ($F = PS_{HMCP} = 5$ PS_{urea}), and high ($F = 0.2$ $PS_{HCMP} = PS_{urea}$) vascular permeability were simulated (Fig. 3). These simulations were also repeated for nonzero blood volume ($v_b = 0.25$). After generating the tracer curves over 60 s at a fine temporal scale (100 ms), data were sampled at the time points specified above, including both the estimated sensitivity variation due to relaxation effects as described above and contamination by Rician noise at expected levels based on in vivo results (noise standard deviation = 2% of peak t-butanol tissue signal). The effects on parameter estimates of varying relaxation (actual tissue relaxation times set ±25% and ±50% expected values) versus perfect compensation were investigated. Perfusion, tracer permeabilities, distribution, and blood volumes were then estimated from these data samples by the nonlinear least squares fitting procedures described above. Each set of conditions was simulated over 500 repetitions with random noise and random variation of the tracer arrival time t_0 over a temporal window of 3 s in order to simulate experimental variation. The means and standard deviations of the absolute percent errors in the parameter estimates were tabulated for each scenario.

RESULTS

MRI Experiments

Due to the periodic SSFP frequency response, ^{13}C nuclei in both HMCP and urea vial phantoms were excited by the RF train with given TR and flip angle, with center frequency near HMCP. The component images appeared side by side along the frequency-encoded dimension. Reconstructed phantom images are shown in Figure 4.

No effects on heart rate or respiration were observed during or after infusions. Tripolarized imaging revealed potentially informative differences in the in vivo distributions among the three tracers, most prominently in the brain. t-Butanol is freely diffusible in brain tissue, while urea crosses the blood brain barrier only about 240× slower than water (8). Therefore, simultaneous imaging of these tracers provides separation of the cerebrovascular and perfused brain tissue compartments. Image data high-lighting the differential diffusivity of the tracers in normal mouse brain tissue is shown in Figure 5. In order of increasing image intensity in brain tissue, the tracers are urea, HMCP, and t-butanol. This differential tracer signal in brain tissue apparent from these images is reflected in the vascular permeability measurements given below.

A set of tripolarized dynamic in vivo images and tissue region of interest curves from a TRAMP mouse are given in Figure 6. With some similarity to the neuroimaging results, preliminary tumor imaging suggests a slightly increased vascular component of the urea signal, which tends to fill more isolated regions of the tumor mass, in contrast with t-butanol and HMCP, which more rapidly fill the entire tumor volume. However, in contrast with the normal brain data, the main finding is that HMCP and urea both exhibit relatively high signal levels in tumor tissue, a result that is reflected quantitatively in the PS products given below.

Simulations

As depicted in Figure 7, the simulations confirmed the ability of perfusion modeling methods to quantitate high, low, and intermediate PS products, in addition to perfusion, based on the shapes of simulated tripolarized dynamic curves. Errors in the estimated blood flows were low and the mean absolute error did not exceed 11%, even with deviation from expected relaxation times of up to ±50%. Errors in tracer PS products were also low except in the high permeability regime, in which there was some systematic underestimation of the true permeabilities, especially for large deviations from expected relaxation times (up to 44% error for the case of 50% overestimation of the true relaxation times). However, although it was difficult to pinpoint the precise value of the PS product in this regime, computed values were correctly much higher than the perfusion. With this exception, errors in estimated relaxation times were reflected mainly only in the computed distribution volumes. For the case of nonzero blood volume ($v_b = 0.25$), there was little effect on estimated perfusion or distribution volumes, but there was some systematic overestimation of tracer permeabilities, especially for low PS conditions. For example, in the low PS condition, the permeability of the least diffusible tracer (urea) was overestimated by 175% on average, and the permeability of HMCP by 35%. Imperfect compensation for relaxation further compounded these errors. However, in all cases perfusion was much higher than these estimated PS values, indicating that the modeling once again correctly categorized the relative levels of F and PS.

Perfusion and Permeability Modeling

Dynamic mouse brain data showed similar characteristics to simulation data in low PS condition (Figure 8), with comparatively large t-butanol signal. Estimated perfusion parameters for normal mouse brain obtained using tripolarized perfusion MRI methods are

summarized in Table 1, along with data from the other mouse tissue types that were modeled. Tumor perfusion parameter images are shown in Figure 9. Across the three TRAMPs, computed mean tumor blood flows per unit tissue volume (57±16 mL/dL/min) were higher than expected for normal tissues in this anatomic region and similar to reported values for tumor tissues based on established methods of measurement (31, 32). Tumor permeability surface products were also high (in excess of 500 mL/dL/min). As shown in Table 1, normal liver tissue displayed intermediate permeabilities between normal brain and tumor tissues, but with greater variation in the results.

DISCUSSION

We have demonstrated simultaneous dynamic multislice imaging of three co-hyperpolarized ^{13}C perfusion MRI contrast agents using a novel, specially designed pulse sequence methodology incorporating efficient balanced SSFP excitation and rapid spectral-spatial readout using multiband frequency encoding. These methods enable both rapid tandem screening of these individual small molecule ^{13}C perfusion agents with varying physiology, and resulting novel multiparametric contrast based on the multiple simultaneous image data sets. Significantly, these HP ^{13}C tracers have negligible acute pharmacological effects at the dosages used in this study, and in particular are not expected to exhibit nephrotoxicity, a major risk associated with other common medical imaging contrast agents (11).

The widely varying physiological characteristics of these three agents provide previously inaccessible, potentially valuable biological data. In particular, the novel contrast can be modeled for the estimation of tissue perfusion and permeability parameters. We measured higher permeability of mouse prostate tumor tissue to urea and HMCP as compared with normal mouse brain and liver. Normal mouse cerebral blood flows measured in this study were somewhat elevated over values obtained using other methods (e.g. radiotracer methods), for example increased 18% over the upper end of the range of cerebral blood flows measured in a recent study (33). This could be due to a vasodilatory effect of isoflurane in our study (34). Unfortunately, the difficulty of obtaining true gold standard measurements of tissue blood flow in mice (i.e. using the method of radioactive microspheres) in our studies and others precludes the ability to confirm these quantitative results. The permeability of normal brain tissue to urea was correctly estimated to be much lower than its permeability to water (35). Estimated permeability-surface product values were also high, consistent with the characteristic hyperpermeability of tumor vasculature. The significance of the PS product estimates will likely vary by tissue according to baseline permeability, as capillary beds have varying permeability to urea (e.g., very low in brain). Simulations showed that relative estimates of both perfusion and permeability are fairly robust to deviation from the expected tracer relaxation values, which mainly affected only the estimated tracer distribution volumes. This is not surprising since the modeling can mistake changes in tissue tracer affinity for tracer decay, which is potentially separable from changes in the dynamic curve shapes that define vessel permeability and perfusion. However, absolute permeability was prone to systematic underestimation in the high permeability regime and potential overestimation in the low permeability regime in the case of nonzero blood volume, indicating that caution should be exercised in the absolute

interpretation of quantitative PS product data. The sensitivity of the absolute parameter measurements to small changes in permeability is likely low.

In terms of other applications, multiagent perfusion imaging could similarly provide new molecular imaging data for isolating vascular and perfused tissue compartments in neuroimaging (e.g., as depicted in Figure 5) and for studying molecular transport mechanisms with high specificity, such as for improved assessment of renal function (16). Illustrating the significance of the tumor imaging example, the efficacy of chemotherapy is known to depend substantially on drug delivery to the tumor within a normal, intact vascular network (36). Existing perfusion imaging methods based on any single tracer are likely to have a more limited ability to distinguish vascular leakage from normal perfusion. Thus, this approach may provide additional information to describe the perfusion and permeability characteristics of tumor vasculature for the purpose of tailoring individual chemotherapeutic regimens. Furthermore, since a perfusion metabolism mismatch is associated with adverse disease features in certain human cancers (37–39), HP ^{13}C perfusion imaging has great synergy with HP ^{13}C metabolic imaging (e.g., with [1-^{13}C]pyruvate), which has been the focus of most prior research on HP ^{13}C methods (40–42).

Quantification of blood flow using conventional perfusion MRI with paramagnetic Gd-chelates is hampered by limited tracer diffusibility, resulting in mixed effects of perfusion and permeability, and difficulty in estimating tracer concentration, especially the critically important arterial input function due to nonlinearity of signal at high tracer concentration (12). In contrast, HP perfusion MRI offers linearity of signal with tracer concentration, increased tracer diffusibility, and the ability to obtain multiagent perfusion contrast in a single acquisition. Estimation of the input function in blood flow PET, on the other hand, is hampered by limited spatial resolution, often necessitating arterial blood sampling to ensure accurate measurement. Not only is HP ^{13}C perfusion MRI capable of higher spatial resolution than PET, mitigating this effect, it also has the significant potential of using other high-resolution ^{1}H MRI contrast (e.g., TOF MRA) to precisely define the input vessel size for better image-derived estimates of arterial concentration. In addition to providing unique information, the use of multiple perfusion tracers also provides a degree of redundancy that suppresses the effects of noise on perfusion modeling. More work is needed to compare our results with existing perfusion imaging methods like dynamic contrast-enhanced or dynamic susceptibility contrast MRI, and blood flow PET, and to validate our approach against existing gold standard methods for measurement of tissue blood flow.

Acknowledgments

We gratefully acknowledge the assistance of Mark Van Criekinge, Christine Leon Swisher, and Ilwoo Park with experiments in this study.

Grant sponsor: NIH; Grant numbers: P41EB013598, R01EB013427, R01CA166655 and R01EB017449.

REFERENCES

1. Ardenkjaer-Larsen JH, Fridlund B, Gram A, Hansson G, Hansson L, Lerche MH, Servin R, Thaning M, Golman K. Increase in signal-to-noise ratio of > 10,000 times in liquid-state NMR. Proc Natl Acad Sci U S A. 2003; 100:10158–10163. [PubMed: 12930897]

2. Golman K, Ardenkjaer-Larsen JH, Petersson JS, Mansson S, Leunbach I. Molecular imaging with endogenous substances. Proc Natl Acad Sci U S A. 2003; 100:10435–10439. [PubMed: 12930896]
3. von Morze C, Larson PE, Hu S, Keshari K, Wilson DM, Ardenkjaer-Larsen JH, Goga A, Bok R, Kurhanewicz J, Vigneron DB. Imaging of blood flow using hyperpolarized [^{13}C]urea in preclinical cancer models. J Magn Reson Imaging. 2011; 33:692–697. [PubMed: 21563254]
4. Johansson E, Månsson S, Wirestam R, Svensson J, Petersson JS, Golman K, Ståhlberg F. Cerebral perfusion assessment by bolus tracking using hyperpolarized ^{13}C. Magn Reson Med. 2004; 51:464–472. [PubMed: 15004786]
5. Svensson J, Månsson S, Johansson E, Petersson JS, Olsson LE. Hyperpolarized ^{13}C MR angiography using trueFISP. Magn Reson Med. 2003; 50:256–262. [PubMed: 12876701]
6. von Morze C, Larson PE, Hu S, Yoshihara HA, Bok RA, Goga A, Ardenkjaer-Larsen JH, Vigneron DB. Investigating tumor perfusion and metabolism using multiple hyperpolarized ^{13}C compounds: HP001, pyruvate and urea. Magn Reson Imaging. 2012; 30:305–311. [PubMed: 22169407]
7. Grant AK, Vinogradov E, Wang X, Lenkinski RE, Alsop DC. Perfusion imaging with a freely diffusible hyperpolarized contrast agent. Magn Reson Med. 2011; 66:746–755. [PubMed: 21432901]
8. Levin VA. Relationship of octanol/water partition coefficient and molecular weight to rat brain capillary permeability. J Med Chem. 1980; 23:682–684. [PubMed: 7392035]
9. Mayrand RR, Levitt DG. Urea and ethylene glycol-facilitated transport systems in the human red cell membrane. Saturation, competition, and asymmetry. J Gen Physiol. 1983; 81:221–237. [PubMed: 6842173]
10. Sands JM, Layton HE. The physiology of urinary concentration: an update. Semin Nephrol. 2009; 29:178–195. [PubMed: 19523568]
11. Maliborski A, Zukowski P, Nowicki G, Boguslawska R. Contrast-induced nephropathy—a review of current literature and guidelines. Med Sci Monit. 2011; 17:RA199–RA204. [PubMed: 21873958]
12. de Langen AJ, van den Boogaart VE, Marcus JT, Lubberink M. Use of H_2 ^{15}O-PET and DCE-MRI to measure tumor blood flow. Oncologist. 2008; 13:631–644. [PubMed: 18586918]
13. Harwood-Nash DC, Lansdown EL. Evaluation of the urea washout pyelogram and urography in the assessment of renovascular hypertension. Can Med Assoc J. 1967; 96:245–256. [PubMed: 6018051]
14. Reed DJ, Woodbury DM. Effect of hypertonic urea on cerebrospinal fluid pressure and brain volume. J Physiol. 1962; 164:252–264. [PubMed: 13973539]
15. McGregor D. Tertiary-Butanol: a toxicological review. Crit Rev Toxicol. 2010; 40:697–727. [PubMed: 20722584]
16. von Morze C, Bok RA, Sands JM, Kurhanewicz J, Vigneron DB. Monitoring urea transport in rat kidney in vivo using hyperpolarized ^{13}C magnetic resonance imaging. Am J Physiol Renal Physiol. 2012; 302:F1658–F1662. [PubMed: 22492940]
17. Wilson DM, Keshari KR, Larson PE, et al. Multi-compound polarization by DNP allows simultaneous assessment of multiple enzymatic activities in vivo. J Magn Reson. 2010; 205:141–147. [PubMed: 20478721]
18. Sourbron SP, Buckley DL. Tracer kinetic modelling in MRI: estimating perfusion and capillary permeability. Phys Med Biol. 2012; 57:R1–R33. [PubMed: 22173205]
19. Cunningham CH, Chen AP, Albers MJ, Kurhanewicz J, Hurd RE, Yen YF, Pauly JM, Nelson SJ, Vigneron DB. Double spin-echo sequence for rapid spectroscopic imaging of hyperpolarized ^{13}C. J Magn Reson. 2007; 187:357–362. [PubMed: 17562376]
20. Hu S, Lustig M, Balakrishnan A, Larson PE, Bok R, Kurhanewicz J, Nelson SJ, Goga A, Pauly JM, Vigneron DB. 3D compressed sensing for highly accelerated hyperpolarized ^{13}C MRSI with in vivo applications to transgenic mouse models of cancer. Magn Reson Med. 2010; 63:312–321. [PubMed: 20017160]
21. Larson PE, Hu S, Lustig M, Kerr AB, Nelson SJ, Kurhanewicz J, Pauly JM, Vigneron DB. Fast dynamic 3D MR spectroscopic imaging with compressed sensing and multiband excitation pulses for hyperpolarized ^{13}C studies. Magn Reson Med. 2011; 65:610–619. [PubMed: 20939089]

22. Lau AZ, Chen AP, Hurd RE, Cunningham CH. Spectral-spatial excitation for rapid imaging of DNP compounds. NMR Biomed. 2011; 24:988–996. [PubMed: 21751271]
23. Mayer D, Yen YF, Tropp J, Pfefferbaum A, Hurd RE, Spielman DM. Application of subsecond spiral chemical shift imaging to real-time multislice metabolic imaging of the rat in vivo after injection of hyperpolarized ^{13}C1-pyruvate. Magn Reson Med. 2009; 62:557–564. [PubMed: 19585607]
24. von Morze C, Reed G, Shin P, Larson PE, Hu S, Bok R, Vigneron DB. Multi-band frequency encoding method for metabolic imaging with hyperpolarized [1-^{13}C]pyruvate. J Magn Reson. 2011; 211:109–113. [PubMed: 21596601]
25. Yen YF, Le Roux P, Mayer D, King R, Spielman D, Tropp J, Butts Pauly K, Pfefferbaum A, Vasanawala S, Hurd R. T_2 relaxation times of ^{13}C metabolites in a rat hepatocellular carcinoma model measured in vivo using ^{13}C-MRS of hyperpolarized [1-^{13}C]pyruvate. NMR Biomed. 2010; 23:414–423. [PubMed: 20175135]
26. Freeman R, Hill HDW. Phase and intensity anomalies in Fourier transform NMR. J Magn Reson. 1971; 4:366–383.
27. Leupold J, Mansson S, Petersson JS, Hennig J, Wieben O. Fast multiecho balanced SSFP metabolite mapping of ^{1}H and hyperpolarized ^{13}C compounds. MAGMA. 2009; 22:251–256. [PubMed: 19367422]
28. von Morze C, Sukumar S, Reed GD, Larson PE, Bok RA, Kurhanewicz J, Vigneron DB. Frequency-specific SSFP for hyperpolarized ^{13}C metabolic imaging at 14.1 T. Magn Reson Imaging. 2013; 31:163–170. [PubMed: 22898680]
29. Mallett CL, Foster PJ. Optimization of the balanced steady state free precession (bSSFP) pulse sequence for magnetic resonance imaging of the mouse prostate at 3T. PLoS One. 2011; 6:e18361. [PubMed: 21494660]
30. Greenberg NM, DeMayo F, Finegold MJ, Medina D, Tilley WD, Aspinall JO, Cunha GR, Donjacour AA, Matusik RJ, Rosen JM. Prostate cancer in a transgenic mouse. Proc Natl Acad Sci U S A. 1995; 92:3439–3443. [PubMed: 7724580]
31. Davies B, Morris T. Physiological-parameters in laboratory-animals and humans. Pharmaceut Res. 1993; 10:1093–1095.
32. Wilson CB, Lammertsma AA, McKenzie CG, Sikora K, Jones T. Measurements of blood flow and exchanging water space in breast tumors using positron emission tomography: a rapid and noninvasive dynamic method. Cancer Res. 1992; 52:1592–1597. [PubMed: 1540969]
33. Xu K, Radhakrishnan K, Serhal A, Allen F, Lamanna JC, Puchowicz MA. Regional brain blood flow in mouse: quantitative measurement using a single-pass radio-tracer method and a mathematical algorithm. Adv Exp Med Biol. 2011; 701:255–260. [PubMed: 21445795]
34. Sicard K, Shen Q, Brevard ME, Sullivan R, Ferris CF, King JA, Duong TQ. Regional cerebral blood flow and BOLD responses in conscious and anesthetized rats under basal and hypercapnic conditions: implications for functional MRI studies. J Cereb Blood Flow Metab. 2003; 23:472–481. [PubMed: 12679724]
35. Takagi S, Ehara K, Finn RD. Water extraction fraction and permeability-surface product after intravenous injection in rats. Stroke. 1987; 18:177–183. [PubMed: 3810751]
36. Jain RK. Normalization of tumor vasculature: an emerging concept in antiangiogenic therapy. Science. 2005; 307:58–62. [PubMed: 15637262]
37. Aronen HJ, Pardo FS, Kennedy DN, Belliveau JW, Packard SD, Hsu DW, Hochberg FH, Fischman AJ, Rosen BR. High microvascular blood volume is associated with high glucose uptake and tumor angiogenesis in human gliomas. Clin Cancer Res. 2000; 6:2189–2200. [PubMed: 10873068]
38. Komar G, Kauhanen S, Liukko K, Seppanen M, Kajander S, Ovaska J, Nuutila P, Minn H. Decreased blood flow with increased metabolic activity: a novel sign of pancreatic tumor aggressiveness. Clin Cancer Res. 2009; 15:5511–5517. [PubMed: 19706808]
39. Mankoff DA, Dunnwald LK, Gralow JR, Ellis GK, Charlop A, Lawton TJ, Schubert EK, Tseng J, Livingston RB. Blood flow and metabolism in locally advanced breast cancer: relationship to response to therapy. J Nucl Med. 2002; 43:500–509. [PubMed: 11937594]

40. Chen AP, Albers MJ, Cunningham CH, et al. Hyperpolarized C-13 spectroscopic imaging of the TRAMP mouse at 3T-initial experience. Magn Reson Med. 2007; 58:1099–1106. [PubMed: 17969006]

41. Golman, K. Real-time metabolic imaging. In: ‘t Zandt, R.; Thaning, M., editors. Proc Natl Acad Sci U S A. Vol. 103. 2006. p. 11270-11275.

42. Schroeder MA, Cochlin LE, Heather LC, Clarke K, Radda GK, Tyler DJ. In vivo assessment of pyruvate dehydrogenase flux in the heart using hyperpolarized carbon-13 magnetic resonance. Proc Natl Acad Sci U S A. 2008; 105:12051–12056. [PubMed: 18689683]

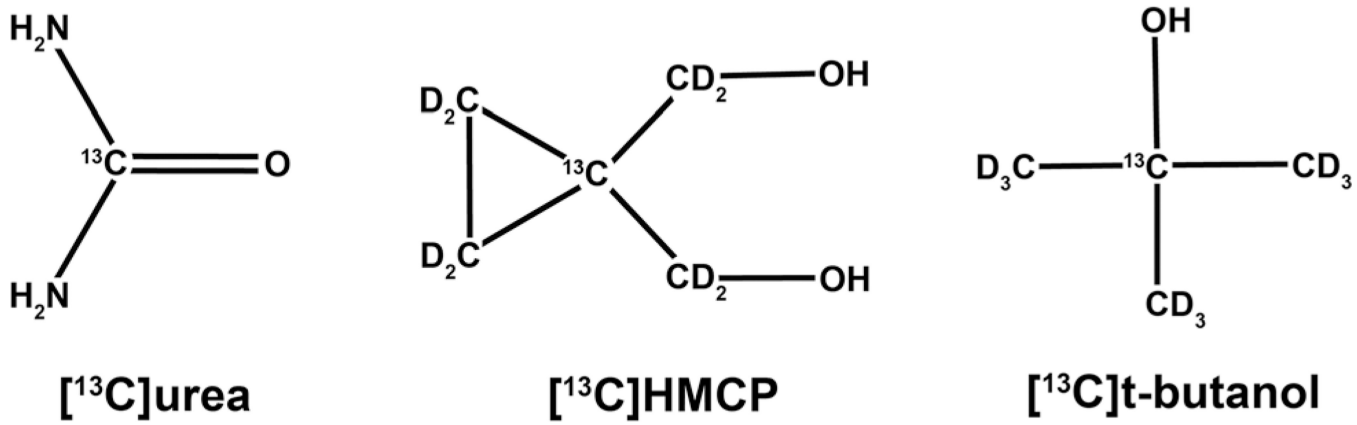

FIG. 1.
Molecular structures of HP ^{13}C perfusion tracers enabled by dissolution DNP.

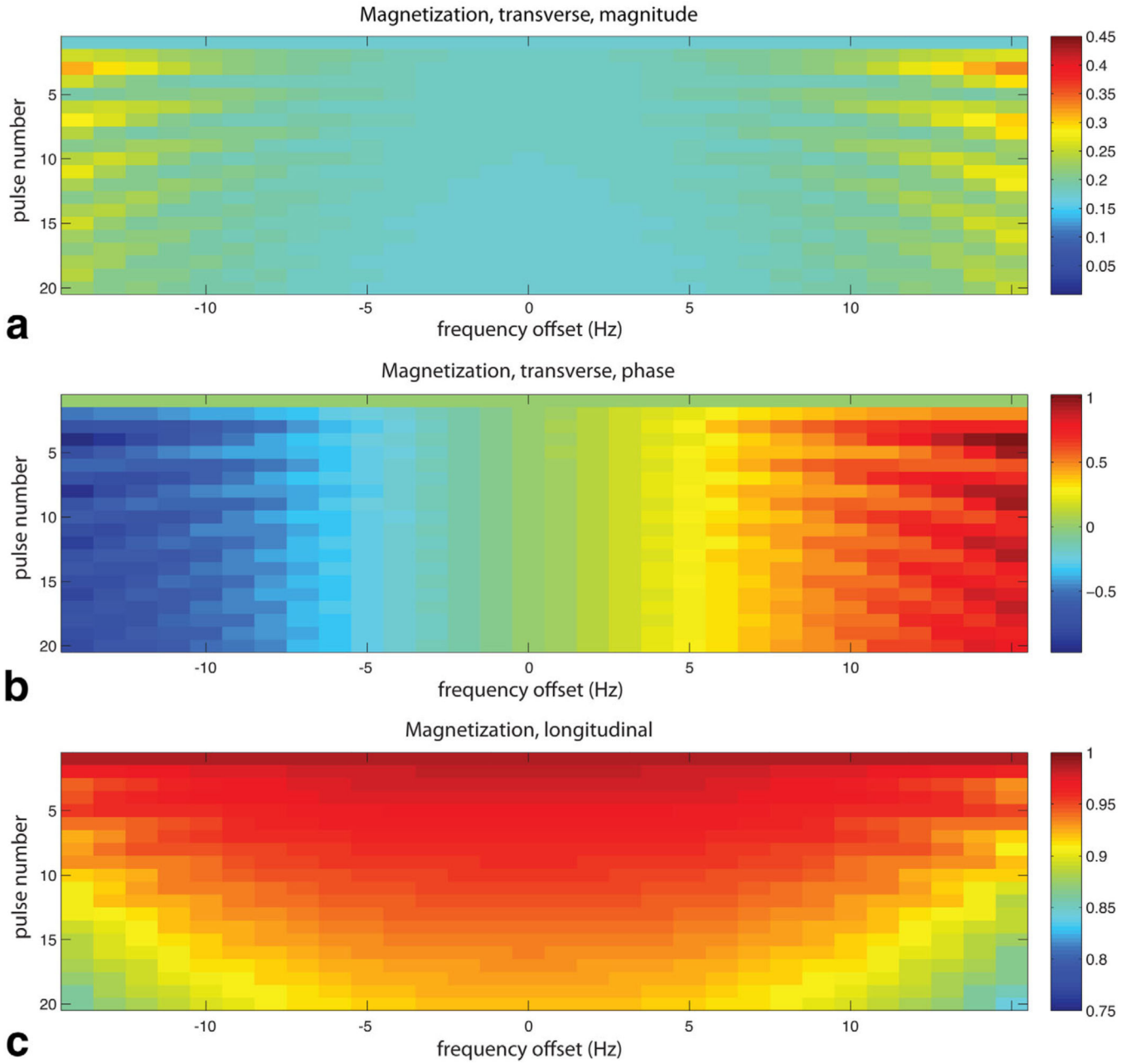

FIG. 2.

Simulated transient response of HP magnetization to SSFP RF pulse train ($\alpha = \pm 20°$) over a 1-ppm range of Larmor frequencies near resonance, in terms of magnetization magnitude (**a**), phase (**b**), and remaining z-component (**c**) as a function of pulse number.

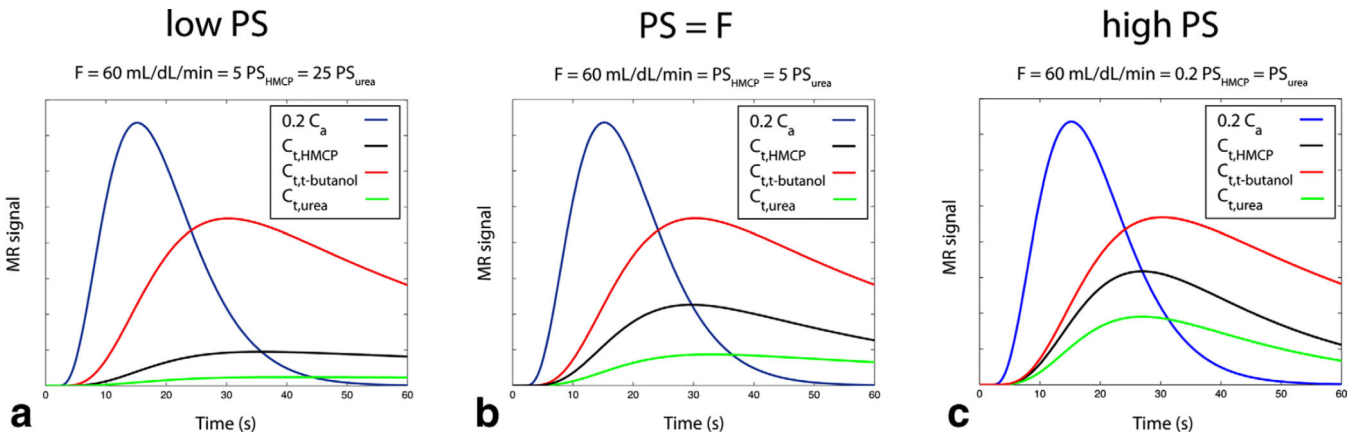

FIG. 3.

Simulated ideal tripolarized arterial (C_a) and tissue (C_t) concentration curves for three scenarios described in text (**a–c**), prior to inclusion of relaxation effects, noise, and randomization of tracer arrival time.

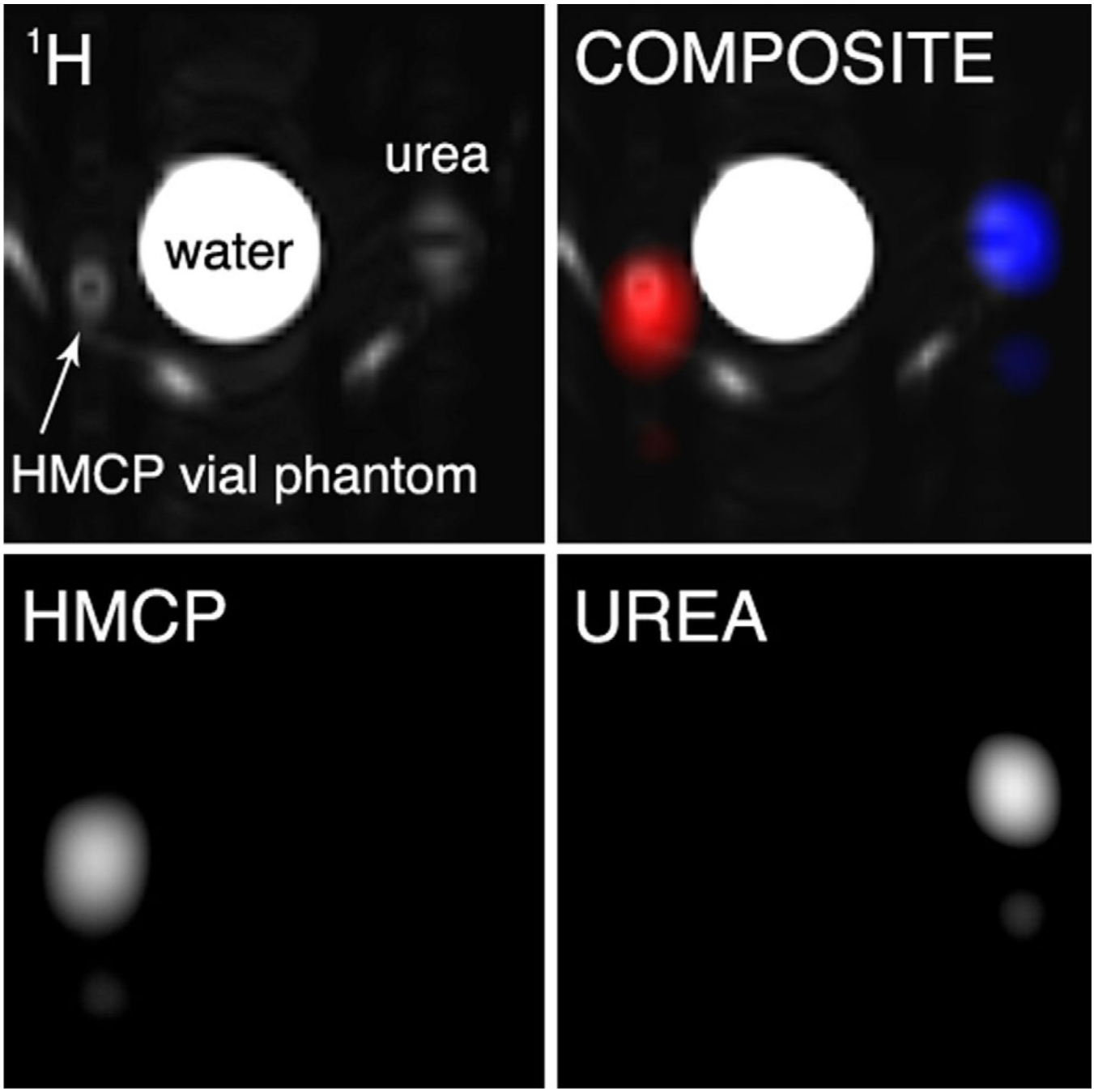

FIG. 4.

Thermal vial phantom images of enriched ^{13}C urea (6 M) and HMCP (5 M), obtained using balanced SSFP excitation with multiband frequency encoding readout. Images include: ^{1}H image (top left), individual ^{13}C images (bottom row), and composite overlay (gray = ^{1}H, blue = urea, red = HMCP). Unlabeled bright areas in ^{1}H image are from a water-heating pad attached to the coil.

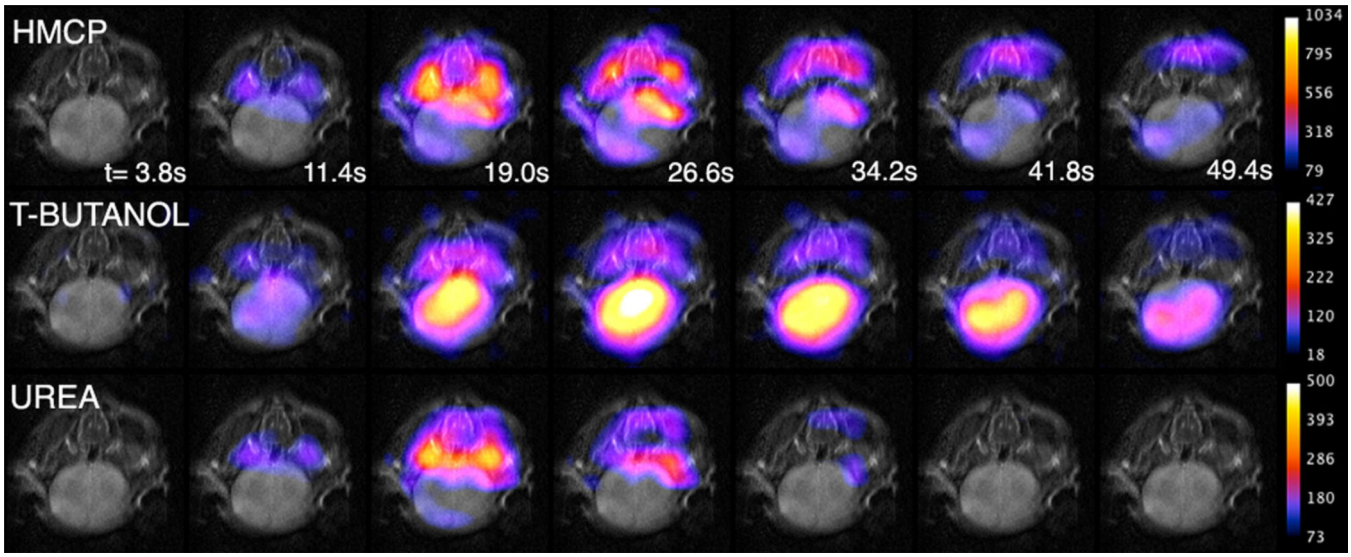

FIG. 5.

Axial tripolarized images of mouse brain (color) overlaid on T_2 images (gray). Images are remarkable for showing that t-butanol rapidly crosses the blood–brain barrier, unlike urea and HMCP.

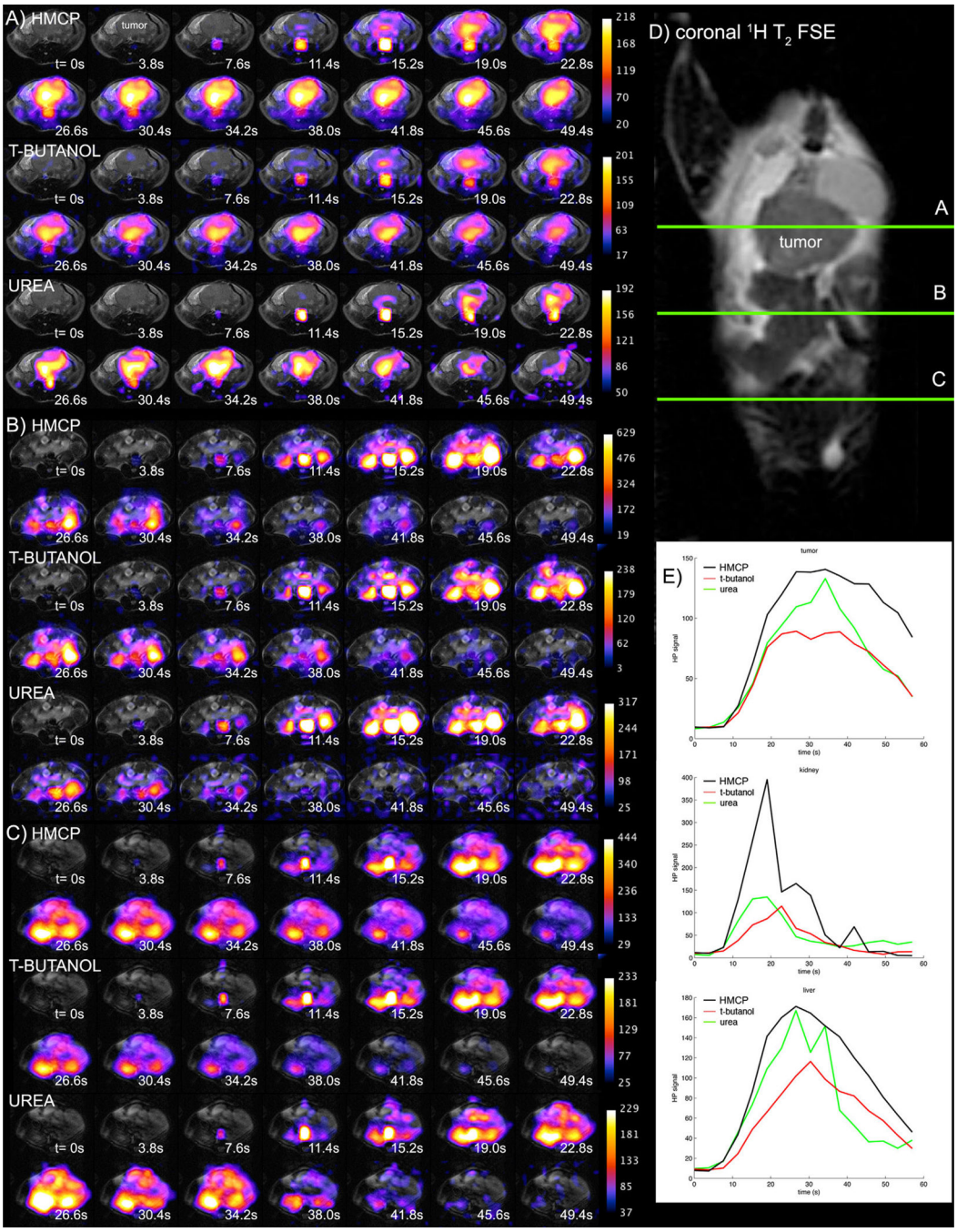

FIG. 6.

Tripolarized ^{13}C dynamic perfusion images (color) from three adjacent axial slices (**a–c**) in TRAMP mouse, overlaid on T_2-weighted fast spin echo ^{1}H images (gray). For optimal contrast, different window-level settings were applied to each image series as indicated by the colorbars on the right. Slice locations are indicated on coronal ^{1}H image (**d**). Mean tissue-specific perfusion curves (**e**) are given for HMCP (black), t-butanol (red), and urea (green), in tumor (top), kidney (middle), and liver (bottom).

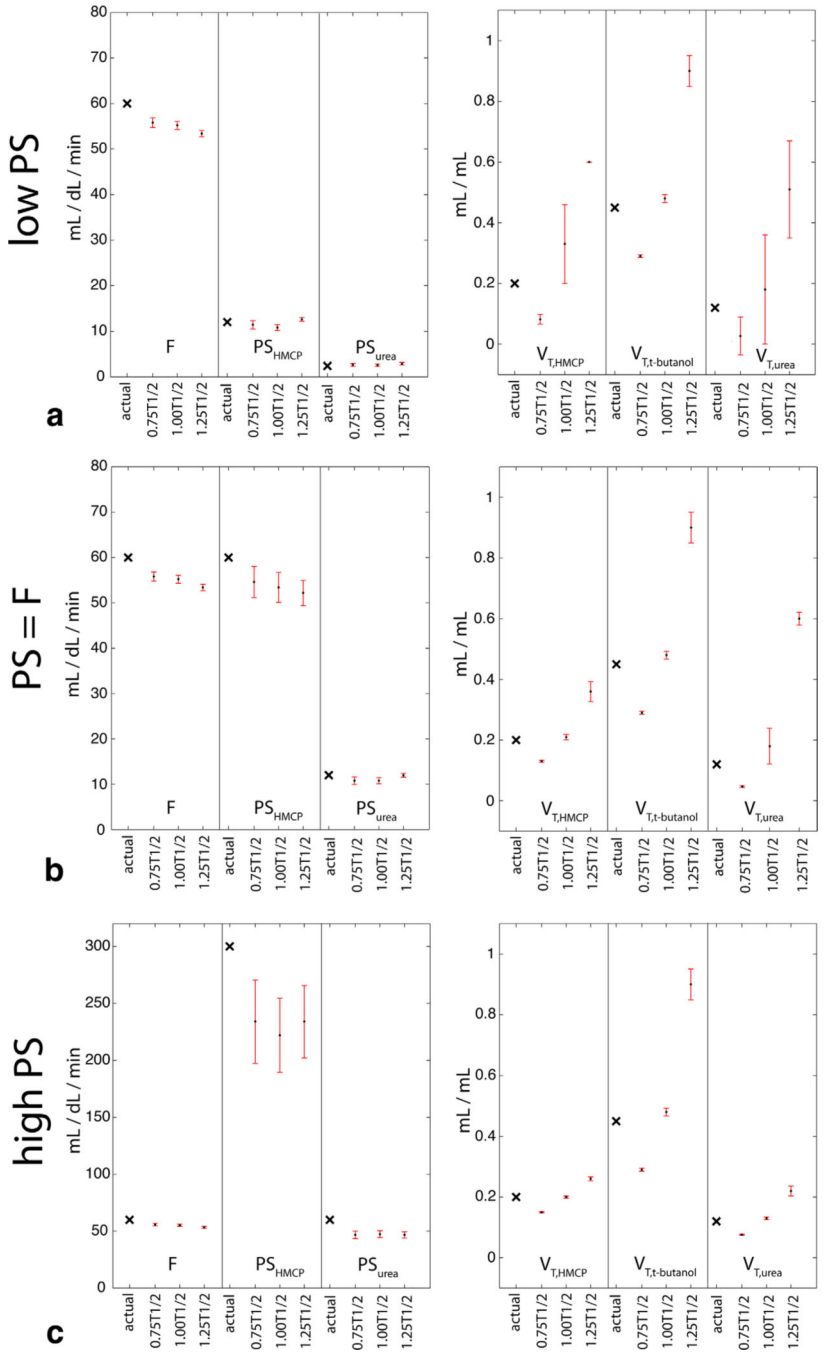

FIG. 7.

Simulated impact of potential relaxation effects on quantitation of perfusion and permeability parameters in three biological regimes as described in text (**a–c**, as shown in Fig. 3). Actual parameter values are marked by a black × in the left-most column of each data set. Shown are the estimated parameter means (black dot)±SDs (upper and lower bounds shown by red error bars) over 500 repetitions with errors in estimated T_1 and T_2 relaxation times of ±25%.

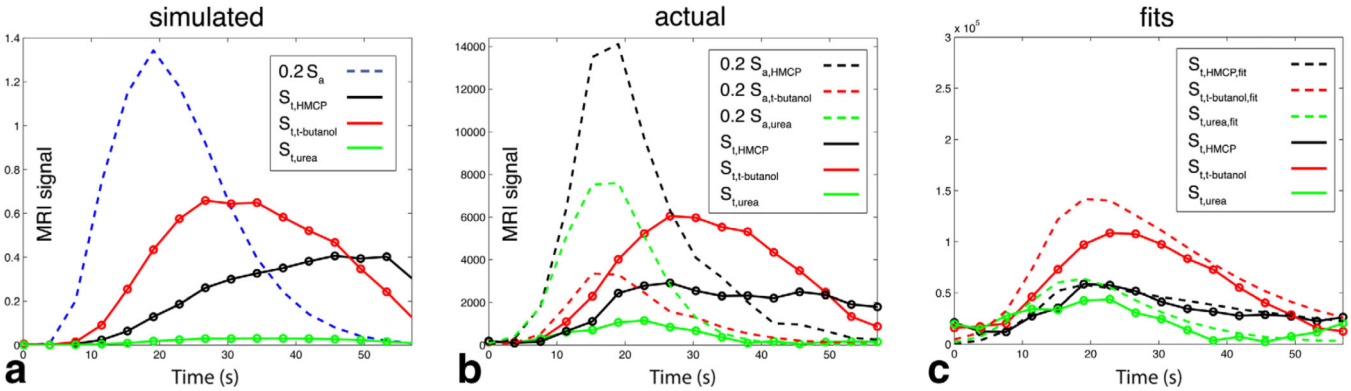

FIG. 8.

Comparison of simulation data (**a**) with actual raw uncorrected in vivo mouse brain dynamic data (**b**) including relaxation effects and noise, under low PS conditions. **c:** Fits of corrected mouse brain tissue data to the model. The selected voxel was from the center of the mouse brain, with estimated F = 220 mL/dL/min, $PS_{urea/HMCP}$ <20 mL/dL/min. The ratio of tissue to arterial signal levels was higher for the in vivo data compared with simulation data due to higher perfusion (F = 220 mL/dL/min versus 60 mL/dL/min for simulations). The single simulated S_a curve depicted in panel A ignores relaxation and therefore reflects the assumed identical arterial concentration for all tracers. The actual individual simulated arterial signal curves differed slightly due to added relaxation and noise.

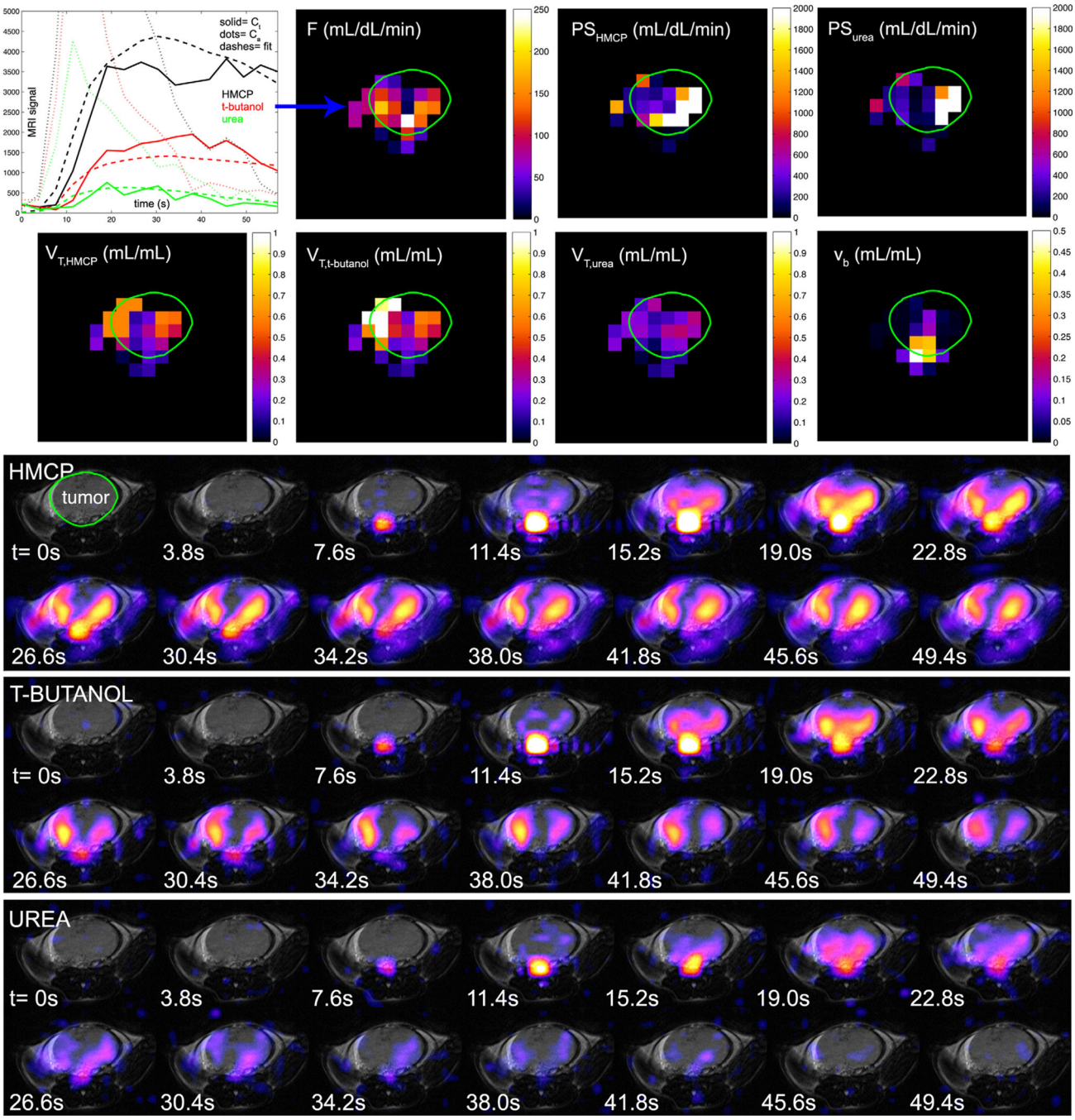

FIG. 9.

Quantification of perfusion and permeability parameters in axial slice through TRAMP tumor based on tripolarized perfusion data. Tumor borders are indicated in green. Dynamic signal curves for the voxel indicated by the blue arrow, estimated blood flow map, tracer permeability surface products, tracer distribution volumes, and blood volume. The mean tumor blood flow was 73 mL/dL/min. Corresponding raw dynamic tripolarized image data

(color), overlaid on anatomic T_2-weighted ^{1}H MRI image for this slice (gray), are shown below.

Table 1

Computed Perfusion and Permeability Parameters for the Three Mouse Tissue Types Investigated

Tissue Type	Parameter					
	F (mL/dL/min)	**PS_{HMCP} (mL/dL/min)**	**PS_{urea} (mL/dL/min)**	**$V_{T,HMCP}$ (mL/mL)**	**$V_{T,t\text{-}butanol}$ (mL/mL)**	**$V_{T,urea}$ (mL/mL)**
Normal brain	200±52	95±54	71±44	0.17±0.12	0.54±0.22	0.06±0.04
Normal liver	26±7.6	380±230	327±270	0.22±0.15	0.07±0.02	0.24±0.12
TRAMP tumor	57±16	730±158	580±250	0.20±0.14	0.25±0.19	0.10±0.07